



Investigations of a Robotic Test Bed With Viscoelastic Liquid Cooled Actuators

Donghyun Kim , Member, IEEE, Junhyeok Ahn, Orion Campbell, Nicholas Paine, Member, IEEE, and Luis Sentis , Member, IEEE

Abstract—We design, build, and thoroughly test a new type of actuator—dubbed viscoelastic liquid cooled actuator (VLCA) for robotic applications. VLCAs excel in the following five critical axes of performance: energy efficiency, torque density, impact resistance, joint position, and force controllability. We first study the design objectives and choices of the VLCA to enhance the performance on the above-mentioned criteria. We follow this study by an investigation on viscoelastic materials in terms of their damping, viscous, and hysteresis properties as well as their long-term performance. As part of the actuator design, we devise a disturbance observer to provide high-fidelity force control for a wide range of impedance control capabilities. We proceed to design a robotic system capable to lift large payloads with high output power. In addition, we experiment with quick trajectory control while carrying moderate payloads. Finally, we perform experiments on impedance control capabilities and mechanical robustness by studying the response of the robot to impacts produced by a hammer and human-induced external forces. Overall the main contribution of this paper is on the invention of a VLCA using elastomers with a pistonlike ball screw drive for multidof robots and the thorough investigation of its robotics performance.

Index Terms—Impedance control, torque feedback control, viscoelastic liquid cooled actuator (VLCA).

I. INTRODUCTION

SERIES elastic actuators (SEAs) [1] have been extensively used in robotics [2], [3] due to their impact resistance and high-fidelity torque controllability. One drawback of SEAs is

Manuscript received November 4, 2017; revised March 8, 2018 and June 29, 2018; accepted September 4, 2018. Date of publication September 26, 2018; date of current version December 13, 2018. Recommended by Technical Editor H. A. Varol. This work was supported in part by the Office of Naval Research under Grant N000141512507, in part by the NASA Johnson Space Center, and in part by the NSF/NASA NRI Grant under Grant NNX12AM03G. (Corresponding author: Luis Sentis.)

D. Kim is with Cockrell School of Engineering, The University of Texas at Austin, Austin, TX 78712 USA (e-mail: dk6587@utexas.edu).

J. Ahn and O. Campbell are with the Department of Mechanical Engineering, The University of Texas at Austin, Austin, TX 78712 USA (e-mail: junhyeokahn91@utexas.edu; orioncampbelliv@gmail.com).

N. Paine is with the Department of Engineering, Appttronik, Austin, TX 78758 USA (e-mail: npaine@appttronik.com).

L. Sentis is with the Department of Aerospace Engineering, The University of Texas at Austin, Austin, TX 78712, USA (e-mail: lsentis@aus.tin.utexas.edu).

This paper has supplementary downloadable material available at <http://ieeexplore.ieee.org>.

Color versions of one or more of the figures in this paper are available online at <http://ieeexplore.ieee.org>.

Digital Object Identifier 10.1109/TMECH.2018.2872176

the difficulty that arises when using a joint position controller due to the presence of the elastic element in the drivetrain. To remedy this problem, the addition of dampers has been previously considered [4]–[6]. However, incorporating mechanical dampers makes actuators bulky and increases their mechanical complexity.

One way to avoid this complexity is to employ elastomers instead of metal springs. Using a viscoelastic material instead of combined spring–damper systems enables compactness [7] and simplifies drivetrains [8]. However, it is difficult to achieve high bandwidth torque control due to the nonlinear behavior of elastomers. To address this difficulty, Austin *et al.* [9] model the force–displacement curve of elastomers using a “standard linear model.” The estimated elastomer force is employed in a closed-loop force controller. Unfortunately, the hysteresis in the urethane elastomer used in the previous work destabilized the system at frequencies above 2 Hz. In contrast, our controllers achieve a bandwidth of 70 Hz. The study in [10] accomplishes reasonably good torque control performance, but the range of achievable torques is small to ensure that the elastomer operates in the linear region; our design and control methods described here achieve more than an order of magnitude higher than the range of torques with high fidelity tracking.

To sufficiently address the nonlinear behavior of elastomers, which can severely reduce force control performance, we empirically analyze various viscoelastic materials using a custom-built elastomer test bed. We measure each material’s linearity, creep, compression set, and damping under preloaded conditions, providing an underdocumented study in the academic literature. To achieve stable and accurate force control, we study various feedback control schemes. In a previous work, we showed that the active passivity obtained from motor velocity feedback [11] and model-based control, such as the use of a disturbance observer (DOB) [12], plays an essential role in achieving high-fidelity force feedback control. Here, we analyze the phase margins of various feedback controllers and empirically show their performance in the new actuator. We verify the stability and accuracy of our controllers by studying impedance control and impact tests.

To test our new actuator, we have designed a two-degrees-of-freedom robotic test bed, as shown in Fig. 5. It integrates two of our new actuators, one in the ankle and another in the knee. With the foot bolted to the floor for initial testing, weight plates can be attached to the hip joint to serve as an end-effector payload. We test operational space control to show stable and

accurate Cartesian impedance behaviors. We perform quick motions with high payloads to showcase another important aspect of our system, which is the effect of the cooling system on significantly increasing the power output.

The torque density of electric motors is often limited by sustainable core temperatures. The maximum continuous torque and periodic peak torques of electric motors can be significantly enhanced using a cooling system. Our previous study [13] analyzed the improvements on achievable output power of a single motor based on thermal data of the electric motor. This study allowed us to propose metrics for the design of the cooling system. Based on these metrics, for this new study, we chose a 120-W Maxon EC-max 40 motor, which we expect to achieve a 2.88 times continuous torque increase when using the liquid cooling system. We demonstrate the effectiveness of liquid cooling by achieving 860 N continuous force during 5 min and 4500 N periodic peak forces at 2 Hz while keeping the core temperatures below 115 °C. In addition, we perform heavy lift tests with a payload of 32.5 kg keeping the motor temperatures under 80 °C.

The main contribution of this paper is the invention of a viscoelastic liquid cooled actuator (VLCA) using elastomers and a pistonlike ball screw drive for applications in multidof robots. A follow-up contribution is the thorough study of the liquid-cooled viscoelastic multidof robot regarding power and torque density, periodic peak torques, control stability, efficiency, impact robustness, endurance during fast movements, and high payload operation. We demonstrate that the use of liquid cooling with the elastomer significantly improves joint position controllability and power density over traditional SEAs. In addition, we extensively study viscoelastic materials for liquid-cooled viscoelastic multidof robots.

II. BACKGROUND

Existing actuators can be characterized using four criteria: power source (electric or hydraulic), cooling type (air or liquid), elasticity of the drivetrain (rigid or elastic), and drivetrain type (direct, harmonic drive, ball screw, etc.). One of the most powerful and common solutions is the combination of hydraulic, liquid cooling, rigid, and direct drive actuation. This achieves high power-to-weight and torque-to-weight ratios, joint position controllability, and shock tolerance. Existing robots that use this type of actuators include Atlas, Spot, Big Dog, and Wildcat of Boston Dynamics, BLEEX of Berkeley [14], and HyQ of the IIT [15]. However, hydraulics are less energy efficient primarily because they require more energy transformations [16]. Typically, a gasoline engine or electric motor spins a pump, which compresses a hydraulic fluid, which is modulated by a hydraulic servo valve, which finally causes a hydraulic piston to apply a force. Each stage in this process incurs some efficiency loss, and the total losses can be very significant.

The combination of electric, air-cooled, rigid, and harmonic drive actuators are other widely used actuation type. Some robots utilizing this combination include Asimo of Honda, HRP2,3,4 of AIST [17], HUBO of KAIST [18], REEM-C of PAL Robotics, JOHNNIE and LOLA of the Technical University of Munich [19], [20], CHIMP of CMU [21], RoboSimian of NASA JPL [22], etc. These actuators have

precise position control and high torque density. Compared to us, low shock tolerance, low-fidelity force sensing, and low-efficiency gearboxes are common drawbacks of this type of actuators. According to Harmonic Drive AG's catalog, the efficiency of harmonic drives may be as low as 25% and only increases above 80% when optimal combinations of input shaft speed, ambient temperature, gear ratio, and lubrication are present. Conversely, the efficiency of our VLCA is consistently above 80% due to the use of a ball screw mechanism.

Urata *et al.* [23] used liquid cooling for electric, rigid, harmonic drive actuators to enhance the continuous power-to-weight ratio. The robots using this type of actuation include SCHAFT and Jaxon [24]. These actuators share the advantages and disadvantages of electric, rigid, harmonic drive actuators, but have a significant increase in the continuous power output and torque density. In contrast to our design, these actuators do not employ viscoelastic materials, reducing their mechanical robustness and high-fidelity force sensing and control.

Although the increased power density achieved via liquid cooling amplifies an electric actuator's power, the rigid drivetrain is still vulnerable to external impacts. To increase impact tolerance, many robots (e.g., Walkman [25] and COMAN of the IIT [26], Valkyrie of the NASA [27], MABEL and MARLO of UMICH [28], [29], TORO of DLR [30], and StarLETH of ETH [31]) adopt electric, air-cooled, elastic, harmonic drive actuators. This type of actuation provides high-quality force sensing, force control, and impact resistance. However, precise joint position control is difficult because of the elasticity in the drivetrain and the coupled effect of force feedback control and real-time latencies [32]. Low efficiency originating from the harmonic drives is another drawback.

As an alternative to harmonic drives, ball screws are great drives for mechanical power transmission. SAFFiR, THOR, and ESCHER of Virginia Tech [33]–[35], M2V2 of IHMC [36], Spring Flamingo of MIT [37], Hume of UT Austin [11], and the X1 Mina exoskeleton of NASA [38] use electric, air-cooled, elastic, ball-screw drives. These actuators show energy efficiency, good power and force density, low-noise force sensing, high-fidelity force controllability, and low backlash. Compared to these actuators, our design significantly reduces the bulk of the overall actuator and increases its joint position controllability. Some other actuators have special features, such as the electric actuators used in MIT's cheetah [39], which allow for shock resistance through a transparent but backlash-prone drivetrain. However, the lack of passive damping limits the joint position controllability of this type of robots compared to ours.

III. VISCOELASTIC MATERIAL CHARACTERIZATION

The most challenging aspect of incorporating elastomers into the structural path of an actuator is estimating or modeling their complex mechanical properties. To address this, we perform experiments to empirically measure the following four properties of our viscoelastic springs: force versus displacement, stress relaxation, compression set, and frequency response, which will be used to characterize each material's effective viscous damping. We built a viscoelastic material test bed, depicted in Fig. 1(a), to measure each of these properties. We selected and

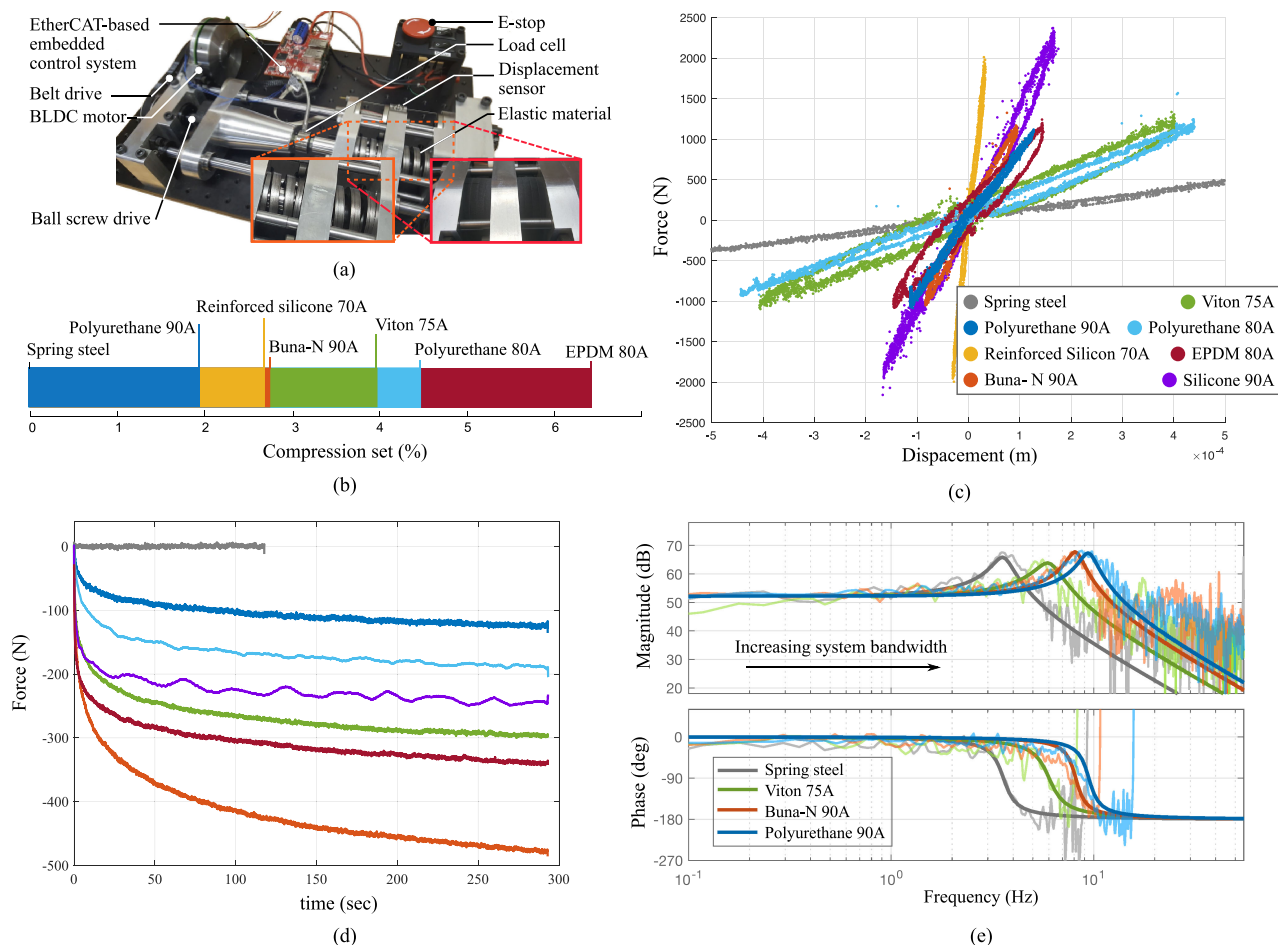


Fig. 1. Viscoelastic material test. (a) Elastomer test bed is designed and built to study various material properties of candidate viscoelastic materials. (b) We measured each elastomer's free length both before and after they were placed in the preloaded test bed. (c) Strong correlation between material hardness and the materials stiffness can be observed. An exception to this correlation is the fabric reinforced silicone that we hypothesize had increased stiffness due to the inelastic nature of its reinforcing fabric. Nonlinear effects, such as hysteresis, can also be observed in this plot. (d) We command a rapid change in material displacement and then measure the materials force change versus time for 300 s. Note that the test of reinforced silicone 70 A is omitted due to its excessive stiffness. (e) Although the bandwidths of the four responses are different, their damping ratios (signal peak values) are relatively constant, which implies different damping.

TABLE I
SUMMARY OF VISCOELASTIC MATERIALS

Materials	Compression set (%)	Linearity (R-square)	Linear stiffness (N/mm)	Creep (%)	Material damping (N s/m)	Part Number (McMaster)	Material Cost (\$)
Spring steel	0	0.996	860.8	0	0	-	-
Polyurethane 90A	2	0.992	8109	15.3	16000	8716K27	19.40
Reinforced silicone 70A	2.7	0.978	57570	-	242000	8612K55	29.08
Buna-N 90A	2.8	0.975	11270	25	29000	80115K161	51.47
Viton 75A	4	0.963	2430	30.14	9000	8625K16	105.62
Polyurethane 80A	4.5	0.993	2266	16.8	4000	8716K27	19.40
EPDM 80A	6.48	0.939	6499	23.4	16000	3727T26	35.28
Silicone 90A	-	0.983	12460	10.7	37000	5773T24	29.41

tested the seven candidate elastomers that are listed in Table I. The dimensions of the tested materials are fairly regular, with 46-mm diameter and 27-mm thickness. In addition to these materials, we also characterized a die spring made from coiled chrome silicon spring steel (Diamond Wire corp.) as a point of comparison.

A. Compression Set

Compression set is the reduction in length of an elastomer after prolonged compression. The drawback of using materials with a compression set in compliant actuation is that the materials must be installed with larger amounts of preload forces to avoid the material sliding out of place during usage. To measure

this property, we measured each elastomer's free length both before and after the elastomer was placed in the preloaded test bed. The result of our compression set experiments are summarized in [Table I](#).

B. Force Versus Displacement

In the design of compliant actuation, it is essential to know how much a spring will compress given an applied force. This displacement determines the required sensitivity of a spring-deflection sensor and also affects mechanical aspects of the actuator, such as usable actuator range of motion and clearance to other components due to Poisson ratio expansion. In this experiment, we identify the force versus displacement curves for the various elastomer springs. Experimental data for all eight springs are shown in [Fig 1\(b\)](#). Note that there is a disagreement between our empirical measurements and the analytic model relating stiffness to hardness, i.e., the Gent's relation presented in [40]. This mismatch arises because in our experiments the materials are preloaded, whereas the analytical models assume unloaded materials.

C. Stress Relaxation

Stress relaxation is an undesirable property in compliant actuators for two reasons. First, the time-varying force degrades the quality of the compliant material as a force sensor. When a material with significant stress-relaxation properties is used, the only way to accurately estimate actuator force based on deflection data is to model the effect and then pass deflection data through this model to obtain a force estimate. This model introduces complexity and more room for error. The second reason stress-relaxation can be problematic is that it can lead to the loss of contact forces in compression-based spring structures.

The experiment for stress relaxation is conducted as follows:

- 1) enforce a desired displacement to a material;
- 2) record the force data over time from the load cell; and
- 3) subtract the initially measured force from all of the force data.

Empirically measured stress-relaxation properties for each of the materials are shown in [Fig. 1\(c\)](#), which represent force offsets as time goes under the same displacement enforced. Note that each material would have a different initial force due to the different stiffness. To have all the plots starting at the zero force level for comparison, we subtract the initial force.

D. Dynamic Response

In regard to compliant actuation, the primary benefit of using elastomer springs is their viscous properties, which shapes the dynamic response of an actuator in series with such a component. To perform this experiment, we generate motor current to follow an exponential chirp signal, using frequencies between 0.001 and 200 Hz. Given the input–output relation of the system, we can fit a second-order transfer function to the experimental data to obtain an estimate of the system's viscous properties. However, this measure also includes the ball screw drive train friction of the viscoelastic test bed [see [Fig. 1\(a\)](#)]. To quantify

the elastomer spring damping independently of the damping of the test bed drive train, the drivetrain friction of 8000 N·s/m was first characterized using a metal spring, and then subtracted from subsequent tests of the elastomer springs to obtain estimates for the viscous properties of the elastomer materials. [Fig. 1\(e\)](#) shows the frequency response results for the current input and force output of three different springs while controlling the damping ratio. The elastomers have higher stiffness than the metal spring, hence their natural frequencies are higher.

E. Selection of Polyurethane 90A

A variety of other experiments were conducted to strengthen our analysis and are summarized in [Table I](#). Based on these results, Polyurethane 90A appears to be a strong candidate for viscoelastic actuators based on its high linearity (0.992), low compression set (2%), low creep (15%), and reasonably high damping (16000 N·s/m). It is also the cheapest of the materials and comes in the largest variety of hardnesses and sizes.

IV. VISCOELASTIC LIQUID COOLED ACTUATION

The design objectives of the VLCA are as follows: power density, efficiency, impact tolerance, joint position controllability, and force controllability. Our previous work [13] shows a significant improvement in motor current, torque, output power, and system efficiency for liquid-cooled commercial off-the-shelf (COTS) electric motors. As an extension of this previous work, in this new study, we study the use of COTS motors and their thermal behavior models, and to that end, we selected the Maxon EC-max 40 brushless 120 W [see [Fig. 2\(d\)](#)]. We then designed and built a custom housing to accommodate the liquid cooling system [see [Fig. 2\(e\)](#)]. As a result of using liquid cooling, we increase the maximum continuous current by a factor of 2.88. Therefore, a continuous motor torque of 0.4 N·m (before gear augmentation) is theoretically achievable. With the use of liquid cooling, this actuator is designed to achieve 294 W continuous power with an 85% ball screw efficiency [see [Fig. 2\(m\)](#)]. This performance translates into a continuous power density of 155.4 W/kg for a total actuator mass of 1.692 kg plus an additional weight of 0.2 kg due to the liquid pump, radiator, and reservoir system. By combining convection liquid cooling and a high-efficiency ball screw, we aim to surpass existing electric actuation technologies in terms of power density.

In terms of controls, a common problem with conventional SEAs is their lack of physical damping at their mechanical output. As a result, active damping must be provided via feedback [41]. However, the presence of signal latency and derivative signal filtering severely limits the amount by which active damping can be increased, resulting in SEA-driven robots achieving only relatively low output impedances [32] and thus operating with limited joint position control accuracy and bandwidth. Our VLCA design incorporates damping directly into the compliant element itself, reducing the requirements placed on active damping efforts from the controller. The incorporation of passive damping aims to increase the output impedance while retaining compliance properties, resulting in higher joint position control bandwidth. The retention of a compliant element in the

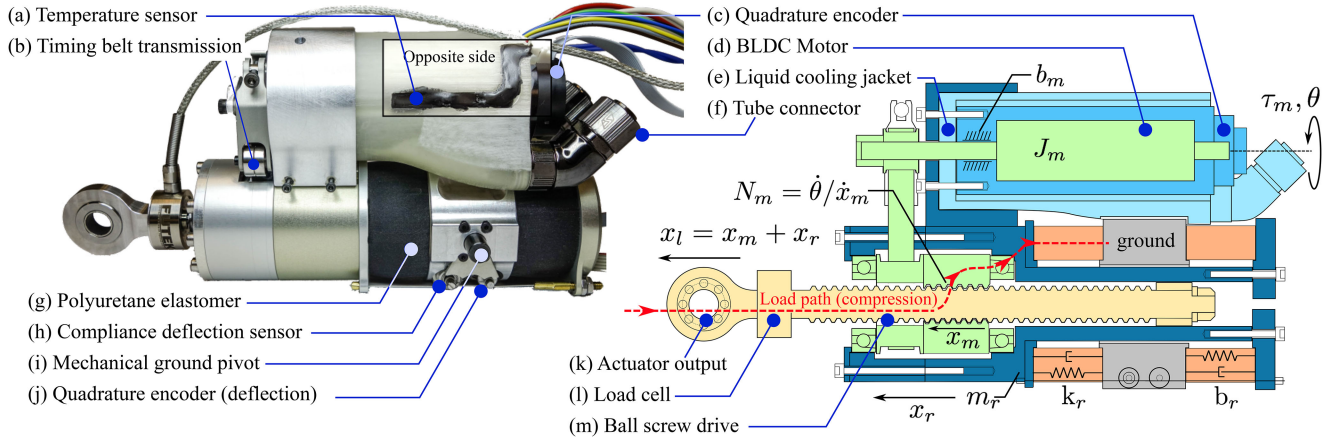


Fig. 2. VLCA. The labels are explanatory. In addition, the actuator contains five sensors: a load cell, a quadrature encoder for the electric motor, a temperature sensor, and two elastomer deflection sensors. One of the elastomer deflection sensors is absolute and the other one is a quadrature encoder. The quadrature encoder gives high-quality velocity data of the elastomer deflection.

VLCA drive enables the measurement of actuator forces based on deflection. The inclusion of a load cell [see Fig. 2(l)] on the actuators output serves as a redundant force sensor and is only required to calibrate the force–displacement characteristics of the viscoelastic element.

Mechanical power is transmitted when the motor turns a ball nut via a low-loss timing belt and pulley [see Fig. 2(b)], which causes the ball screw to exert a force to the actuator’s output [see Fig. 2(k)]. The rigid assembly consisting of the motor, ball screw, and ball nut connects in series to the compliant viscoelastic element [see Fig. 2(g)], which connects to the mechanical ground of the actuator [see Fig. 2(i)]. When the actuator exerts a force, it causes the viscoelastic element to compress. The viscoelastic element enables the actuator to be more shock tolerant than rigid actuators yet also enables high output impedance due to the inherent damping in the elastomer that increases controller stability.

V. ACTUATOR FORCE FEEDBACK CONTROL

To demonstrate various impedance behaviors in operational space, robots must have an effective force controller. We therefore extensively study various types of force feedback controllers. The first step is to identify the actuator dynamics. The transfer function related to the reaction force sensed in the SEA (elastomer deflection) is well explained in [42]. When the actuator output is fixed, the transfer function from the motor current input to the elastomer deflection is given by

$$P_x = \frac{x_r}{i_m} = \frac{\eta k_\tau N_m}{(J_m N_m^2 + m_r)s^2 + (b_m N_m^2 + b_r)s + k_r} \quad (1)$$

where η , k_τ , N_m , and i_m are the ball screw efficiency, the torque constant of the motor, the speed reduction ratio of the motor provided by the ball screw, and the current input to the motor, respectively. The equations of this section will follow the nomenclature in Fig. 3(a). We can find η , k_τ , and N_m in the product data sheets, being 0.9, 0.0448 N·m/A, and 3316, respectively. The gear ratio of the drivetrain is computed by dividing

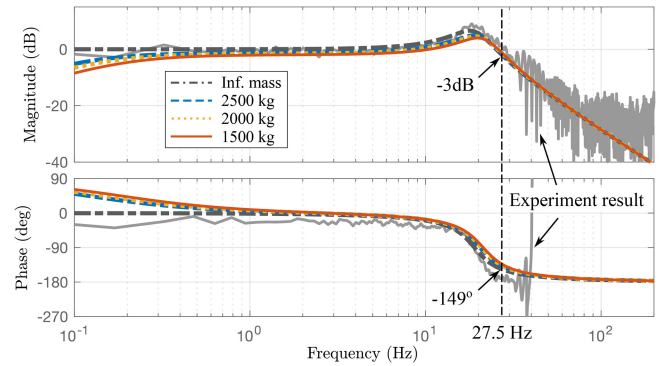


Fig. 3. Frequency response of the VLCA. A gray solid line shows model-free experimental data, whereas the other lines are estimations using a model with parameters obtained from empirical measurements.

TABLE II
ACTUATOR PARAMETERS

J_m (kg m ²)	b_m (N m s)	m_r (kg)	b_r (N s/m)	k_r (N/m)
3.8e-5	2.0e-4	1.3	2.0e4	5.5e6

the speed reduction of the pulley (2.111) with the lead length of the ball screw (0.004 m) via the equation $2\pi \times 2.111/0.004$.

However, for our model, we need to experimentally identify k_r , b_r , J_m , and b_m . We infer k_r by dividing force measurements from the load cell by elastomer deflections. The other three parameters are estimated by comparing the frequency response of the model to the experimental data. The force-based frequency response test is done using the ankle actuator while blocking joint movement. The results are shown in Fig. 3 via a solid gray line. Note that the dotted gray lines correspond to the estimated response from the transfer function (measured elastomer force/input motor force) using the parameters of Table II. The estimated response and experimental results match closely with one another, suggesting that the parameters we found are close to the actual values.

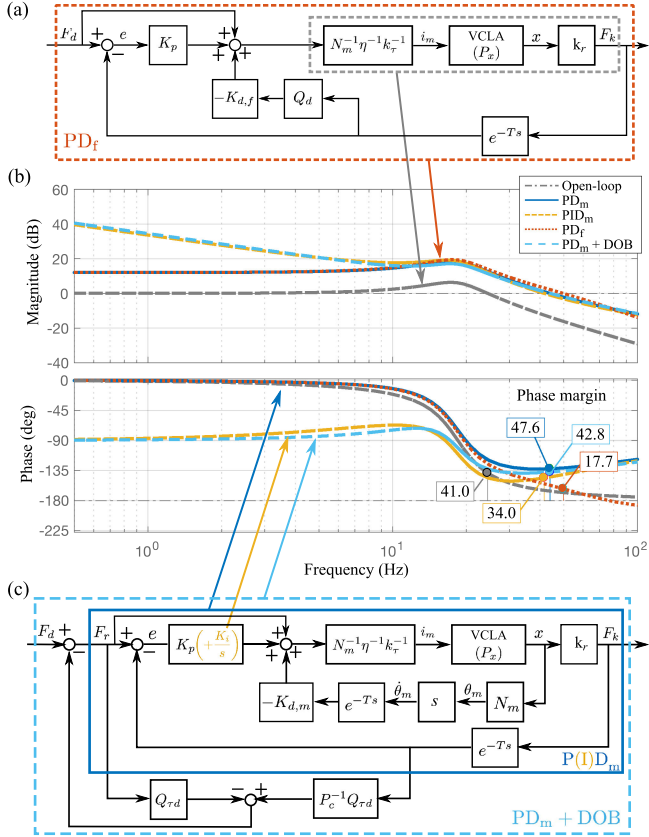


Fig. 4. Stability analysis of force controllers. Phase margins of each controller and the open-loop system response are presented.

We also study the frequency response for different load masses to understand how the actuator dynamics changes as the joint moves. When 10 kg is attached to the end of the link, the reflected mass on the actuator varies from 1500 to 2500 kg because the length of the effective moment arm changes depending on the position of the joint. Fig. 3(b) depicts the resulting bode plots. The response does not vary significantly from the fixed output case. Therefore, we design feedback controllers based on the fixed output dynamics as a general case.

For the force feedback controller, we first compare two options, which we have used in our previous studies [11], [12]: proportional (P) + derivative (D_f) control using velocity signal obtained by a low-pass derivative filtered elastomer deflection; and proportional (P) + derivative (D_m) control using motor velocity signal measured by a quadrature encoder connected to the motor axis. The second controller (PD_m) has benefits over the first one (PD_f) with respect to sensor signal quality. The velocity of the motor is directly measured by a quadrature encoder rather than low-pass filtered elastomer deflection data, the latter being relatively more noisy and lagging in phase. In addition, Fig. 4 shows that the phase margin of the second controller (47.6°) is larger than the first one (17.1°).

To remove the force tracking error at low frequencies, we consider two options: augmenting the controller either with integral control PID_m or with a DOB $PD_m + DOB$ controller. To compare the two controllers, we analyze their phase margins. Let us derive the closed-loop transfer function for the PD_f

controller as follows:

$$F_k = \frac{k_r P_x}{N} (k_p (F_r - e^{-T_s} F_k) + F_r - k_{d,f} Q_d e^{-T_s} F_k) \quad (2)$$

where F_k , F_r , T , and Q_d are the measured force from an elastomer deflection, a reference force, a time delay, and a low-pass derivative filter, respectively. For convenience, we use N as a replacement for the product $\eta k_r N_m$. The above equation can be written as

$$\frac{F_k}{F_r} = \frac{k_r P_x (K_p + 1)/N}{1 + e^{-T_s} k_r P_x (K_p + K_{d,f} Q_d)/N}. \quad (3)$$

Then, the open-loop transfer function of the closed system with the time delay is given as

$$P_{PD_f}^{\text{open}} = k_r P_x (K_p + K_{d,f} Q_d)/N. \quad (4)$$

We can apply the same method for the PID_m and $PD_m + DOB$ controllers. The transfer function for PID_m , as shown in Fig. 4(c), is given as follows:

$$\frac{F_k}{F_r} = \frac{k_r P_x (K_p + K_i/s + 1)/N}{1 + e^{-T_s} P_x (k_r (K_p + K_i/s) + K_{d,m} s N_m)/N}. \quad (5)$$

When we apply a DOB instead of integral control, we need the inverse of this plant. In our case, the plant of the DOB for PD_m is similar to the above equation except that K_i and e^{-T_s} are omitted

$$P_{PD_m} (= P_c) = \frac{k_r P_x (K_p + 1)}{N + P_x (k_r K_p + K_{d,m} s N_m)}. \quad (6)$$

The formulation of PD_m including the DOB, as shown in Fig. 4(c), is

$$\begin{aligned} \frac{F_k}{F_d} &= \frac{k_r P_x (K_p + 1)}{N(1 - Q_{\tau d}) + e^{-T_s} (N Q_{\tau d} + P_x (k_r K_p + K_{d,m} s N_m))} \end{aligned} \quad (7)$$

where $Q_{\tau d}$ is a second-order low-pass filter. The open-loop transfer function is given as

$$P_{PD_m + DOB}^{\text{open}} = \frac{N Q_{\tau d} + P_x (k_r K_p + K_{d,m} s N_m)}{N(1 - Q_{\tau d})} \quad (8)$$

The bode plots of $P_{PD_f}^{\text{open}}$, $P_{PD_m}^{\text{open}}$, $P_{PID_m}^{\text{open}}$, and $P_{PD_m + DOB}^{\text{open}}$ are shown in Fig. 4(b). The gains (K_p , $K_{d,m}$, K_i) are the same as the values that we use in the experiments shown in Section VII-A, being 4, 15, and 300, respectively. The PD_f controller uses $K_d N_m / k_r$ for $K_{d,f}$ to normalize the derivative gain. The cutoff frequency of the DOB is set to 15 Hz because this is where the $PD_m + DOB$ displays a magnitude trend similar to the integral controller (PID_m). The results imply that the $PD_m + DOB$ controller is more stable than PID_m in terms of their phase margins and maximum phase lag. This analysis is also experimentally verified in Section VII-A.

VI. ROBOTIC TEST BED

We designed and built a robotic test bed (see Fig. 5) consisting of two VLCAs—one for the ankle (q_0) and one for the knee

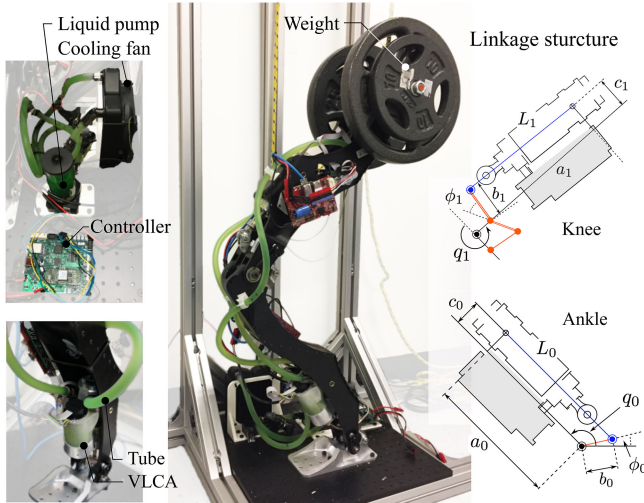


Fig. 5. Robotic test bed. Our test bed consists of two VLCAs driving the ankle and the knee joints. The foot of the test bed is fixed to the ground. The linkages are designed to vary the maximum achievable peak torques and velocities depending on the robot configuration. As the joint positions change, the ratios between ball screw velocities ($\dot{L}_{0,1}$) and joint velocities ($\dot{q}_{0,1}$) also change because the effective lengths of the moment arms vary. The linkages are designed to exert more torque when the robot crouches, which is the posture where gravitational load on the joints is large.

(q_1). The design constrains the robot's motion to the sagittal plane. The robot carries weights of 10, 23, or 32.5 kg at the hip linkage, and its foot is fixed on the ground. With this test bed, we demonstrate coordinated position control with two VLCAs, liquid cooling on the articulated platform, Cartesian position control with various payloads, and verification of the linkage design.

The two joints each have a different linkage structure that was carefully designed so that the moment arm accommodates the expected torques and joint velocities as the robot posture changes. For example, each joint can exert a peak torque of approximately 270 N·m and the maximum joint velocity ranges between 7.5 and 20+ rad/s depending on the mechanical advantage of the linkage along the configurations. The joints can exert a maximum continuous torque of 56 N·m at the point of highest mechanical advantage. This posture dependent ratio of torque and velocity is a unique benefit of prismatic actuators.

Given Cartesian motion trajectories, being second-order B -splines or sinusoidal functions, a centralized controller computes the torque commands based on operational space position and velocity as a function of the sensed joint position and velocity measurements. The operational space control (OSC) formulation that we use is

$$\tau = \mathbf{A} \mathbf{J}_{\text{hip}}^{-1} (\ddot{\mathbf{x}}^{\text{des}} + K_p \mathbf{e} + K_d \dot{\mathbf{e}} - \dot{\mathbf{J}}_{\text{hip}} \dot{\mathbf{q}}) + \mathbf{b} + \mathbf{g} \quad (9)$$

where \mathbf{A} , \mathbf{b} , and \mathbf{g} represent inertia, coriolis, and gravity joint torque, respectively. $\ddot{\mathbf{x}}^{\text{des}}$, \mathbf{e} , and $\dot{\mathbf{e}}$ are desired trajectory acceleration and position and velocity errors, respectively. $\dot{\mathbf{q}} \in \mathcal{R}^2$ is the joint velocity of the robot and τ is the joint torque. \mathbf{J}_{hip} is a Jacobian of the hip linkage, consisting of a 2×2 square matrix and assumed to be full rank.

VII. RESULTS

We first conducted various single actuator tests to show basic performance such as torque and joint position controllability, continuous and peak torque, and impact resistance. Subsequently, we focused on the performance of OSC using the robotic test bed integrated with the DOB-based torque control. Also, we tested various payload lifting capabilities at different speeds to demonstrate actuator efficiency and high power motions.

A. Single Actuator Tests

Fig. 6(a) shows the experimental results of our frequency response tests as well as the estimated response based on the transfer functions. We compare three types of controllers: PD_m , PID_m , and $\text{PD}_m + \text{DOB}$. As we predicted in the analysis of Section V, the $\text{PD}_m + \text{DOB}$ controller shows less phase drop and overshoot than PID_m . The integral control feedback gain used in the experiment is 300 and the cutoff frequency of the DOB's $Q_{\tau d}$ filter is 60Hz, which shows similar error to the PID_m controller [see **Fig. 6(b)**]. The step response shown in **Fig. 6(c)** also validates the stability and accuracy of our torque controller by showing a small overshoot, fast settling time, and zero steady-state error.

Fig. 6(d) is the step response of a joint position controller showing that VLCAs have better joint position controllability than SEAs using metal springs. In the experiment, we use a joint encoder for position control and a motor quadrature encoder for velocity feedback. To compare the VLCAs performance with that of spring-based SEAs, we show simulation results for a spring-based SEA on the same plot as the experiment result for the VLCA. The green dashed line is the simulated step response of our actuator, and the yellow dotted line is the result of the simulation model using the same parameters except for the spring stiffness and damping. The spring stiffness was selected to be 11% of the elastomer's stiffness based on the results of our tests in Section III. The feedback gains are tuned to have the same rise time to each other, and the simulation results confirm that SEAs using a metal spring displays much larger overshoot and longer settling time, which verifies the important benefit of using elastomers for joint position control. The experimental data show longer settling time than the simulation because of a small mechanical backlash in the linkage structure (see **Fig. 5**).

Fig. 6(e) shows the continuous force and the motor core temperature trend with and without liquid cooling. The observed continuous force is 860 N and the motor core temperature settles at 115 °C with liquid cooling, which is a little smaller than the theoretically expected value, 1121 N. **Fig. 6(f)** is the result of a peak torque test. In the experiment, we fix the output of the actuator and command a 31 A current for 0.5 s. The observed force measured by the load cell [see **Fig. 2(l)**] is 4500 N. Again, note that the core temperature is around 107 °C, which is much smaller than the temperature limit to provide a safety margin.

Fig. 7 shows load cell and elastomer force data from the impact tests on a single actuator fixed to a table. In these tests, we hit the actuator shaft [see **Fig. 2(k)**] with a hammer via an

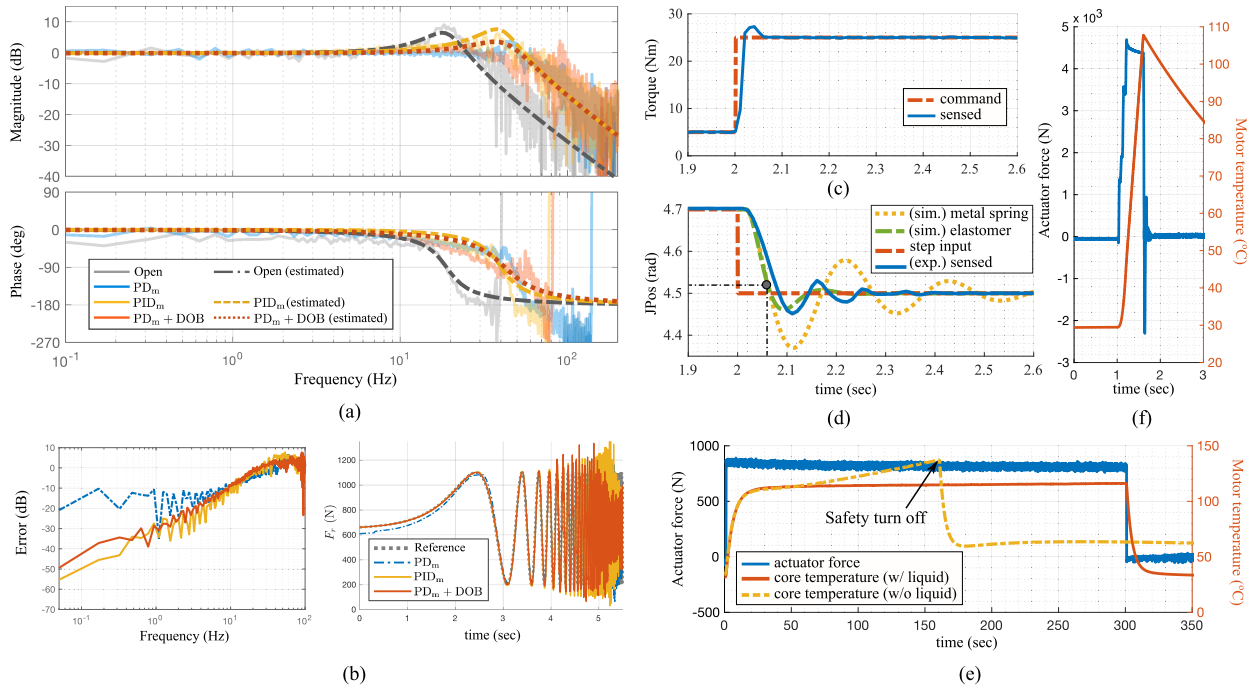


Fig. 6. Single actuator tests. (a) Experimental and estimated data based on the sensed force versus the desired force. The plot indicates that the experimental PD+DOB controller achieves better performance in terms of overshoot and phase drop near the natural frequency than integral control. (b) Left figure shows that the error achieved when using DOB versus integral control is almost the same. The right figure confirms the effectiveness of DOB in the time domain by showing a good tracking performance. (c) Experimental step-response performance when using a torque tracking controller based on PD+DOB. (d) Both experimental and simulated step-response performances when using a simple PD joint position controller. It shows that using the elastomer reduces the oscillatory behavior. (e) Experimental temperature variations when applying a continuous force to the actuator. (f) Experimental temperature variations when applying a short-time peak force.

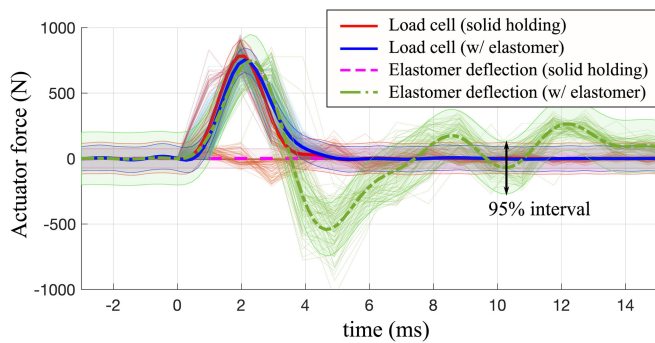


Fig. 7. Impact test. In total 83 trials are plotted and estimated with a Gaussian process. We can see the deflections of the elastomer, which imply that the elastic element absorbs the external impact force.

impulse provided by swinging the hammer in free fall. We mechanically fix the actuator in two different places to compare the behavior of a rigid setup with respect to the viscoelastic actuator response. In the rigid scenario, the outer case corresponding to the dark blue part in Fig. 2 is mechanically fixed to bypass the elastomer from the external impact force path. In the second case, we fix the ground pin of the actuator [see Fig. 2(i)] to observe how the elastomers react to the impact.

The analysis of the impact experiment is challenging because the number of data points we can obtain is very small with a 1 ms update rate. To overcome the lack of data points, we estimate the mean and variance of 83 trials by Gaussian process

regression. The results shown in Fig. 7 imply that there is no significant difference in the forces measured by the load cell in both cases, which is predictable because the elastic element is placed behind the drivetrain. However, the elastomer does play a significant role in absorbing energy from the impact which is evident from large elastomer deflection in the second case. Thus, the presence of the elastic element mitigates the propagation of an impulse to the link where the actuator ground resides.

B. Operational Space Impedance Control

Fig. 8 shows our OSC experimental tests while carrying a 10-kg weight. In the tests, we use the OSC controller presented in Section VI to compute torque commands to achieve a desired Cartesian space motion and PD_m + DOB force control for each joint to track the torque commands. In the first test shown in Fig. 8(a), the commanded behavior is designed to be compliant in the horizontal direction (x) and stiff in the vertical direction (y). When pushing the hip with a sponge in the x direction, the robot smoothly moves rocks back and forth to comply with the push, but it strongly resists vertical disturbances to keep the commanded height. To show the stability of our controller, we also test the response to impacts by hitting the hip's weight with a hammer [see Fig. 8(b)]. Even when there are sudden disturbances, the torque controllers rapidly respond to maintain good torque tracking performance, as shown in Fig. 6(d). Fig. 8(c) shows the tracking performance of our system while

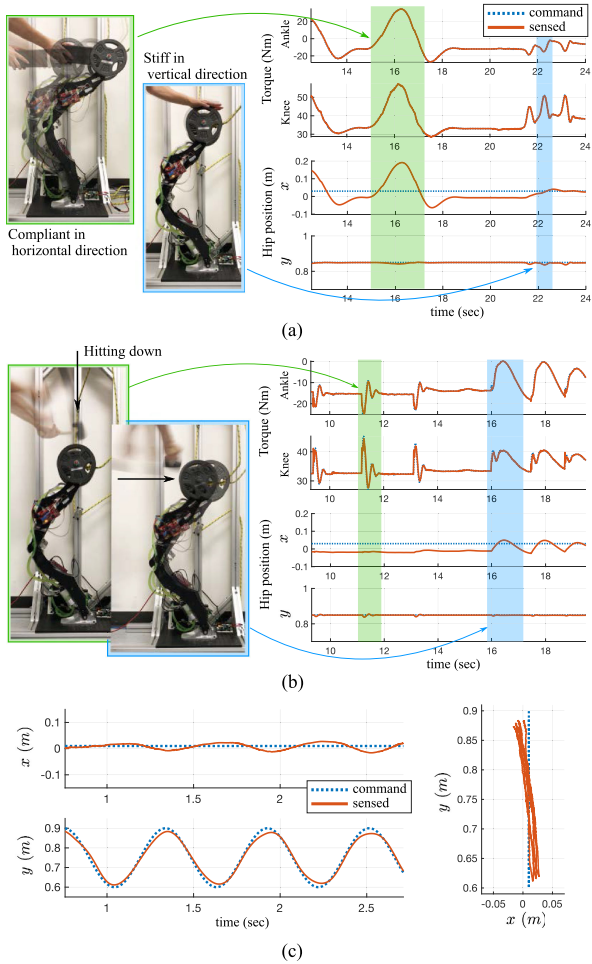


Fig. 8. Operational space impedance control test. (a) Robot achieves directional closed-loop impedance behaviors: stiff in the vertical direction and compliant in the horizontal direction. (b) To demonstrate stability, we hit the weight attached to the robot's hip with a hammer while performing impedance control. Even under the impact, the force controller on the robot shows stability and accurate torque tracking. (c) Robot shows a 0.3 m of amplitude vertical motion trajectory at 1.7 Hz frequency.

following a fast vertical hip trajectory. While traveling 0.3 m with 1.7 Hz frequency, the hip position errors are bounded by 0.025 m. This result demonstrates that our system is capable of stable and accurate OSC.

C. Efficiency Analysis

Fig. 9 explains the power flow from the power supply to the robot joints. Input current (I_b) and voltage (V_b) are measured in the microcontrollers and the product of those two yields the input power from the power supply. $\dot{\theta}_m$ is measured by the quadrature encoder connected to the motor's axis [see Fig. 2(c)] and τ_m is computed from $k_\tau \dot{i}_m$ with \dot{i}_m measured in the microcontroller. Joint velocity is derived by low-pass derivative filtering the joint positions measured using the absolute joint encoders. The torque (τ_k) is computed from projecting the load cell data across the linkage's effective moment arm.

In this test, the robot lifts a 23-kg load with five different durations to study efficiency over a range of speeds and torques. The results are shown in Fig. 9 with the depiction of three different power measures. The sensed torque data measured

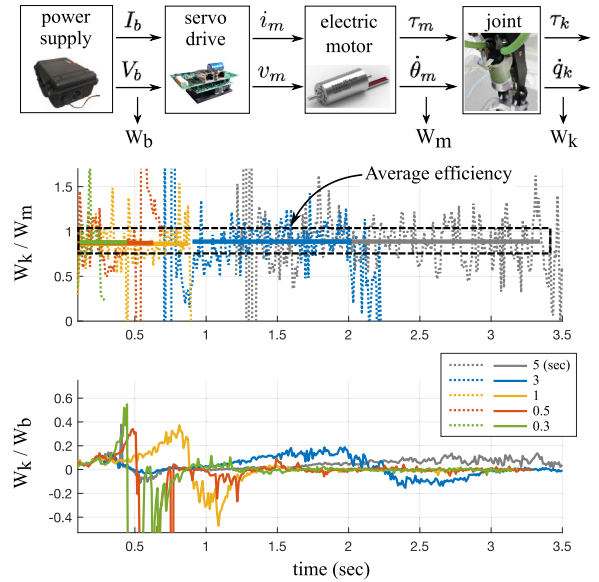


Fig. 9. Efficiency analysis of the ankle actuator. The efficiency of the mechanical system using electrical power has three stages from the power supply to the robot joints. The graph shows the ratio of the mechanical power at the ankle joint and the motor power and the ratio of the joint power and power supply's input power.

by a load cell is noisy; therefore, we compute the average of the drivetrain efficiency for a clearer comparison. The averages are the integrations of efficiency divided by the time durations. Here, we only integrate efficiency while the mechanical power is positive, to prevent confounding our results by incorporating the work done by gravity.

The experimental results show that the drivetrain efficiency is approximately 0.89, which means that we lose only a small amount of power in the drivetrain and most of the torque from the motor is delivered to the joint. This high efficiency indicates only minor drivetrain friction, which is beneficial for dynamics-based motion control.

D. High-Power Motion Experiment

To demonstrate high-power motions, such as fast vertical trajectories and heavy payload lifts, we use the motor position control mode, which uses the quadrature encoders attached directly to the motor for feedback. Fig. 10(a) shows the core temperatures of a test comprised of 1-Hz vertical motion with 0.32 m of travel while carrying a load of 10 kg at the hip. The results show significant improvement because of liquid cooling by demonstrating a 4-min-long fast periodic motion. Fig. 10(b) shows the results of the same test with higher speed (2 Hz). In this test, the knee joint repeatedly exerts 250 N·m, which converts to 132-N·m/kg peak torque density. As for mechanical power, we observed 305 W, which is close to the predicted constant power (300 W). Although the limited range of motion makes it hard to analyze continuous mechanical power, these results convincingly support our claim of enhanced power and torque enabled through liquid cooling. Fig. 10(c) shows another test in which the robot lifts a 32.5-kg weight. We can see that the robot operates in the safe region (≤ 5900 N and ≤ 155 °C) while achieving a high power motion.

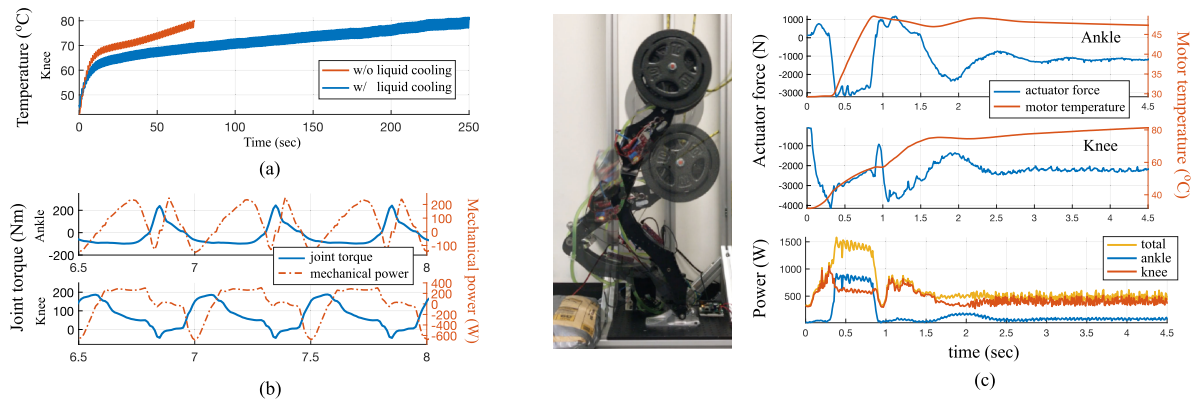


Fig. 10. High-power motion experiment. (a) In this experiment, the robot is commanded to move upwards quickly (0.5 s) from a crouch position and then contract quickly to the crouch position while holding a weight of 10 kg. As it can be seen, liquid cooling significantly reduces the core temperature. (b) In the fast vertical test, the maximum observed torque of the ankle joint is 250 N·m and the maximum observed mechanical power of the knee joint is 310 W. (c) Robot lifts a 32.5-kg load by 0.3 m during 0.4 s. There is still a safety margin with respect to the limits equal to 5900 N and 155 °C.

VIII. CONCLUDING REMARKS

Overall our main contribution has been on the design and extensive testing of a new VLCA for robots. The use of liquid cooling has allowed to sustain high output torque for prolonged times, as shown in the experiments of Fig. 6(e). The use of elastomers versus steel springs has demonstrated a clear improvement on joint position performance, as shown in Fig. 6(d). This capability is important to achieve a large range of output joint or Cartesian space impedances.

One characteristic of other robots that use harmonic drives is that they seem to achieve high peak torque density. For example, the theoretical peak torque density of LOLA, TORO, and Walkman are 129 N·m/kg, 85.35 N·m/kg, and 135 N·m/kg, respectively. Those are comparable to our peak torques, 132 N·m/kg, but one big difference with our approach is that we validate peak torques experimentally and while performing quick periodic motions similar to locomotion patterns (see Fig. 10). In contrast, the literature on these other robots shows neither experimental data nor performance during quick periodic motions. We note that periodic peak torques are an important data point since the actuators endure harder temperature cycles than performing a motion only once.

In the future, we will explore to further reduce the size of our VLCA. While maintaining the current compact design structure, we can still reduce another significant percentage the bulk of the actuator by exploring new types of bearings, ballnut sizes, and piston bearings at the front end of the actuator. We will also explore the use of different materials for the liquid cooling actuator jacket. The current polyoxymethylene material is easily breakable and develops cracks due to the vibrations and impacts of this kind of robotic applications. In the future, we will switch to sealed metal chambers for instance.

ACKNOWLEDGMENT

The authors would like to thank the members of the Human Centered Robotics Laboratory, The University of Texas at Austin for their help and support.

REFERENCES

- [1] G. A. Pratt and M. M. Williamson, "Series elastic actuators," in *Proc. IEEE/RSJ Int. Conf. Intell. Robots Syst. Hum. Robot Interact. Cooperative Robots*, 1995, pp. 399–406.
- [2] B. Henze, M. A. Roa, and C. Ott, "Passivity-based whole-body balancing for torque-controlled humanoid robots in multi-contact scenarios," *Int. J. Robot. Res.*, vol. 35, no. 12, pp. 1522–1543, Jul. 2016.
- [3] N. Paine *et al.*, "Actuator control for the NASA-JSC Valkyrie humanoid robot: A decoupled dynamics approach for torque control of series elastic robots," *J. Field Robot.*, vol. 32, no. 3, pp. 378–396, May 2015.
- [4] J. Hurst, A. Rizzi, and D. Hobbelen, "Series elastic actuation: Potential and pitfalls," in *Proc. Int. Conf. Climbing Walking Robots*, 2004, pp. 1–6.
- [5] N. Kashiri, G. A. Medrano-Cerda, N. G. Tsagarakis, M. Laffranchi, and D. Caldwell, "Damping control of variable damping compliant actuators," in *Proc. IEEE Int. Conf. Robot. Automat.*, 2015, pp. 850–856.
- [6] C.-M. Chew, G.-S. Hong, and W. Zhou, "Series damper actuator: A novel force/torque control actuator," in *Proc. 4th IEEE/RAS Int. Conf. Humanoid Robots*, 2004, pp. 533–546.
- [7] D. Rollinson *et al.*, "Design and architecture of a series elastic snake robot," in *Proc. IEEE/RSJ Int. Conf. Intell. Robots Syst.*, 2014, pp. 4630–4636.
- [8] K. Abe, T. Suga, and Y. Fujimoto, "Control of a biped robot driven by elastomer-based series elastic actuator," in *Proc. 12th IEEE Int. Workshop Adv. Motion Control*, 2012, pp. 1–6.
- [9] J. Austin, A. Schepelmann, and H. Geyer, "Control and evaluation of series elastic actuators with nonlinear rubber springs," in *Proc. IEEE/RSJ Int. Conf. Intell. Robots Syst.*, 2015, pp. 6563–6568.
- [10] D. Rollinson, S. Ford, B. Brown, and H. Choset, "Design and modeling of a series elastic element for snake robots," in *Proc. ASME Dyn Syst. Control Conf.*, 2013, Paper DSCC2013-3875.
- [11] D. Kim, Y. Zhao, G. Thomas, B. R. Fernandez, and L. Sentis, "Stabilizing series-elastic point-foot bipeds using whole-body operational space control," *IEEE Trans. Robot.*, vol. 32, no. 6, pp. 1362–1379, Dec. 2016.
- [12] N. Paine, S. Oh, and L. Sentis, "Design and control considerations for high-performance series elastic actuators," *IEEE/ASME Trans. Mechatronics*, vol. 19, no. 3, pp. 1080–1091, Jun. 2014.
- [13] N. Paine and L. Sentis, "Design and comparative analysis of a retrofitted liquid cooling system for high-power actuators," *Actuators*, vol. 4, no. 3, pp. 182–202, 2015.
- [14] A. B. Zoss, H. Kazerooni, and A. Chu, "Biomechanical design of the Berkeley lower extremity exoskeleton (BLEEX)," *IEEE Trans. Mechatronics*, vol. 11, no. 2, pp. 128–138, Apr. 2006.
- [15] C. Semini, "Hyq—Design and development of a hydraulically actuated quadruped robot," Ph.D. dissertation, Univ. Genoa, Genoa, Italy, 2010.
- [16] P. A. Bhounsule *et al.*, "Low-bandwidth reflex-based control for lower power walking: 65 km on a single battery charge," *Int. J. Robot. Res.*, vol. 33, no. 10, pp. 1305–1321, 2014.
- [17] N. Kanehira *et al.*, "Design and experiments of advanced leg module (HRP-2l) for humanoid robot (HRP-2) development," in *Proc. Int. Conf. Intell. Robots Syst.*, 2002, vol. 3, pp. 2455–2460.

- [18] I.-W. Park, J.-Y. Kim, J. Lee, and J.-H. Oh, "Mechanical design of humanoid robot platform KHR-3 (KAIST humanoid robot 3: HUBO)," in *Proc. 5th Int. Conf. Humanoid Robots*, 2005, pp. 321–326.
- [19] M. Gienger, K. Löffler, and F. Pfeiffer, "Towards the design of a biped jogging robot," in *Proc. Int. Conf. Robot. Automat.*, 2001, vol. 4, pp. 4140–4145.
- [20] S. Lohmeier, T. Buschmann, H. Ulbrich, and F. Pfeiffer, "Modular joint design for performance enhanced humanoid robot LOLA," in *Proc. Int. Conf. Robot. Automat.*, 2006, pp. 88–93.
- [21] A. Stentz *et al.*, "Chimp, the CMU highly intelligent mobile platform," *J. Field Robot.*, vol. 32, no. 2, pp. 209–228, 2015.
- [22] S. Karumanchi *et al.*, "Team RoboSImian: Semi-autonomous mobile manipulation at the 2015 DARPA robotics challenge finals," *J. Field Robot.*, vol. 34, no. 2, pp. 305–332, 2017.
- [23] J. Urata, Y. Nakanishi, K. Okada, and M. Inaba, "Design of high torque and high speed leg module for high power humanoid," in *Proc. Int. Conf. Intell. Robots Syst.*, 2010, pp. 4497–4502.
- [24] K. Kojima *et al.*, "Development of life-sized high-power humanoid robot JAXON for real-world use," in *Proc. 15th Int. Conf. Humanoid Robots*, 2015, pp. 838–843.
- [25] F. Negrello *et al.*, "A modular compliant actuator for emerging high performance and fall-resilient humanoids," in *Proc. IEEE-RAS 15th Int. Conf. Humanoid Robots (Humanoids)*, 2015, pp. 414–420.
- [26] N. G. Tsagarakis, S. Morfey, G. M. Cerda, L. Zhibin, and D. G. Caldwell, "COMpliant huMANoid COMAN: Optimal joint stiffness tuning for modal frequency control," in *Proc. Int. Conf. Robot. Automat.*, 2013, pp. 673–678.
- [27] N. A. Radford *et al.*, "Valkyrie: NASA's first bipedal humanoid robot," *J. Field Robot.*, vol. 32, no. 3, pp. 397–419, 2015.
- [28] J. W. Grizzle, J. Hurst, B. Morris, H.-W. Park, and K. Sreenath, "MABEL, a new robotic bipedal walker and runner," in *Proc. Amer. Control Conf.*, 2009, pp. 2030–2036.
- [29] A. Ramezani, "Feedback control design for Marlo, a 3D-bipedal robot," Ph.D. dissertation, Mech. Eng., Univ. Michigan, Ann Arbor, MI, USA, 2013.
- [30] J. Engelsberger *et al.*, "Overview of the torque-controlled humanoid robot TORO," in *Proc. IEEE-RAS 14th Int. Conf. Humanoid Robots*, 2014, pp. 916–923.
- [31] M. Hutter, C. Gehring, M. Bloesch, C. D. Remy, R. Y. Siegwart, and M. A. Hoepflinger, C. D. Remy, and R. Siegwart, "StarlETH: A compliant quadrupedal robot for fast, efficient, and versatile locomotion," *Adaptive Mobile Robotics.*, Singapore: World Scientific, 2012, pp. 483–490.
- [32] Y. Zhao, N. Paine, K. Kim, and L. Sentis, "Stability and performance limits of latency-prone distributed feedback controllers," *IEEE Trans. Ind. Electron.*, vol. 62, no. 11, pp. 7151–716, Nov. 2015.
- [33] D. Lahr, V. Orekhov, B. Lee, and D. Hong, "Early developments of a parallelly actuated humanoid, SAFFiR," in *Proc. ASME Int. Des. Eng. Tech. Conf. Comput. Inf. Eng. Conf.*, 2013, Paper DETC2013-12590.
- [34] B. Lee, C. Knabe, V. Orekhov, and D. Hong, "Design of a human-like range of motion hip joint for humanoid robots," in *Proc. Int. Des. Eng. Tech. Conf. Comput. Inf. Eng. Conf.*, Aug. 2014, Paper DETC2014-35214.
- [35] C. Knabe *et al.*, "Design of a series elastic humanoid for the DARPA robotics challenge," in *Proc. 15th Int. Conf. Humanoid Robots (Humanoids)*, 2015, pp. 738–743.
- [36] J. Pratt and B. Krupp, "Design of a bipedal walking robot," *Proc. SPIE*, vol. 6962, pp. 69 621F1–69 621F13, 2008.
- [37] J. E. Pratt, "Exploiting inherent robustness and natural dynamics in the control of bipedal walking robots," Ph.D. dissertation, Mass. Inst. Technol., Cambridge, MA, USA, 2000.
- [38] R. Rea, C. Beck, R. Rovekamp, M. Diftler, and P. Neuhaus, "X1: A robotic exoskeleton for in-space countermeasures and dynamometry," in *Proc. AIAA SPACE 2013 Conf. Expo., AIAA SPACE Forum*, 2013, Paper AIAA 2013-5510.
- [39] S. Seok *et al.*, "Design principles for energy-efficient legged locomotion and implementation on the MIT Cheetah robot," *IEEE Trans. Mechatronics*, vol. 20, no. 3, pp. 1117–1129, Jun. 2015.
- [40] E. Pucci and G. Saccomandi, "A note on the Gent model for rubber-like materials," *Rubber Chem. Technol.*, vol. 75, no. 5, pp. 839–852, 2002.
- [41] M. Hutter, C. D. Remy, M. A. Hoepflinger, and R. Siegwart, "High compliant series elastic actuation for the robotic leg ScarlETH," in *Proc. Int. Conf. Climbing Walking Robots*, 2011, Paper EPFL-CONF-175826.
- [42] Y. Park, S. Oh, and H. Zoe, "Dynamic analysis of reaction force sensing series elastic actuator as unclumped two mass system," in *Proc. 42nd Ann. Conf. IEEE Ind. Electron. Soc.*, 2016, pp. 5784–5789.



real-time constraints.



for high-performance exoskeletons.

Mr. Campbell was the recipient of the Virginia & Ernest Cockrell, Jr., Fellowship in Engineering.



Donghyun Kim (S'16–M'18) received the B.S. degree from Korea Advanced Institute of Science and Technology, Daejeon, South Korea, in 2007, the M.S. degree from Seoul National University, Seoul, South Korea, in 2012, and the Ph.D. degree from The University of Texas at Austin, Austin, TX, USA, in 2017, all in mechanical engineering.

His research interests include dynamic motion control, agile locomotion, whole body control, and state estimation of legged systems with

Junhyeok Ahn received B.S. degree in mechanical engineering from Hanyang University, Seoul, South Korea, in 2016. He is currently working toward the Ph.D. degree in mechanical engineering at The University of Texas at Austin, Austin, TX, USA.

His research interests include robust control of actuators and real-time planning and control synthesis for humanoid robot.

Orion Campbell received the B.S. degree in mechanical engineering from The University of Texas at Austin, Austin, TX, USA, in 2013. He is currently working toward the Ph.D. degree in mechanical engineering at the Human-Centered Robotics Lab, The University of Texas at Austin.

He recently joined Apptrotronik Systems, Austin, TX, USA, as a Software and Controls Engineer. His research interests include whole-body control architectures, trajectory planning for agile humanoid behaviors, and transparency control

Nicholas Paine (S'12–M'15) received the B.S., M.S., and Ph.D. degrees in electrical engineering from the University of Texas at Austin, Austin, TX, USA, in 2008, 2010, and 2014 respectively.

He was a Postdoctoral Researcher in the Human Centered Robotics Lab, the University of Texas in 2015. He cofounded Apptrotronik Systems in 2016, where he is currently the Chief Technology Officer.

Dr. Paine was the recipient of the Virginia & Ernest Cockrell, Jr., Fellowship in Engineering in 2008.

Luis Sentis (S'04–M'17) received the M.S. and Ph.D. degrees in electrical engineering from Stanford University, Stanford, CA, USA, where he developed leading work in theoretical and computational methods for the compliant control of humanoid robots.

He is currently an Associate Professor in aerospace engineering at The University of Texas at Austin (UT Austin), Austin, TX, USA, where he directs the Human Centered Robotics Laboratory. He was UT Austin's Lead for DARPA's Robotics Challenge entry with the NASA Johnson Space Center in 2013. His research focuses on foundations for the compliant control of humanoid robots, algorithms to generate extreme dynamic locomotion, and building robots for educating students in mechatronics.